Supersonic Inlet Study Using the Navier-Stokes Equations

Louis G. Hunter,* John M. Tripp,† and Douglas G. Howlett‡
General Dynamics Corporation, Fort Worth, Texas

The three-dimensional, unsteady, compressible Navier-Stokes equations were numerically solved for the flowfield about three external-compression inlet configurations. Configuration 1 was a generic Mach 2.2 variable-geometry, two-ramp inlet with a bleed slot. Configuration 2 was an F-16/79 inlet at Mach 2.0 with porous-ramp and slot bleed. For these configurations, two different approaches were used to model the bleed. Configurations 1 and 2 were modeled by using three lateral planes in the three-dimensional code with symmetry around the center plane, which provides an equivalent two-dimensional solution. Configuration 3 was an axisymmetric spike inlet at Mach 2.2 at 0 deg angle of attack. A full three-dimensional solution was obtained for this configuration. For configurations 2 and 3, the computed surface pressures are in good agreement with the experimental data for cases with and without bleed. The computed pressure recovery at the throat for the three-dimensional spike inlet at $A_0/A_i = 0.84$ was 2% higher than the compressor-face data. In all the configurations, a computational flow plug was used for the duct outflow boundary. This flow plug eliminates the need to specify a back pressure, particularly at angles of incidence, where the back pressure varies circumferentially. Due to limited computer resources, the analysis was limited to the shock system plus 25-45% of the subsonic diffuser length. Numerical results are given in terms of Mach number and static pressure plots and are compared with experimental data.

Nomenclature

A_o/A_i	= mass flow ratio
C_v	= specific heat at constant volume
e	= specific internal energy, C_vT
E	= total internal energy
F,G,H	= vector flux
M	= Mach number
P,P_T	= static and total pressure
q	= heat flux
R	= gas constant
s	= entropy
T	= static temperature
u,v,w	= Cartesian velocity components
U	= vector of dependent variables $[\rho,\rho u,\rho v,\rho w,\rho E]$
x,y,z	= Cartesian coordinates
α	= angle of attack
γ	= ratio of specific heats
μ,μ_t	= molecular and turbulent viscosity coefficients, respectively
μ_{t_i},μ_{t_o}	= inner and outer turbulent viscosity coefficients, respectively
ξ,η,ζ	= transformed body fitted coordinates
ρ	= density
σ,τ	= viscous stress tensors
θ	= circumferential position

I. Introduction

EXTERNAL-COMPRESSION inlets are used on the majority of existing high-performance supersonic aircraft. During the development cycle of these inlets, substantial wind tunnel testing is required to validate the performance of the air induction system and to identify any potential problems. Not only is wind tunnel testing costly, but scheduling a block of testing time is becoming more difficult when answers are required on a timely basis. In addition, only a small portion of the flowfield in the inlet is instrumented, which has traditionally been the compressor face with a limited number of rakes in the entrance region. The sparse test data often fail to explain some of the complex phenomena occurring in the entrance region of the inlet. This lack of data becomes more critical for low-radar cross-section inlets. These problems, along with increasing costs for models and testing, are driving the industry toward increased use of computational analysis for inlet design.

The HOTOL[1] (horizontal takeoff satellite launcher) has an external compression inlet that will operate at very high Mach numbers. Vehicles in this design category will require computational fluid dynamics (CFD) analysis due to a lack of suitable wind tunnel resources.

Knight[2] performed early supersonic inlet computations using the two-dimensional Navier-Stokes equations. He used two overlapping grids placed over the centerbody and in the duct. The external shock structure was not modeled. His work was limited by computer resources.

Many CFD inlet analyses used today[3-6] are zonal techniques, with the zones normally divided into supersonic, transonic, and subsonic regions. This zonal approach is good for supersonic regions, but has limitations in the regions where the normal shock interacts with both the upstream oblique shock and the downstream subsonic flow. This region is highly elliptic and is strongly influenced by the downstream throttle setting.

The nonzonal method of Campbell and Syberg[7] used a two-dimensional Navier-Stokes code to analyze an external-compression inlet at Mach 1.2. Their work emphasized the entrance region of the inlet with the shock/boundary-layer/bleed interaction. Newsome[8] used the two-dimensional Navier-Stokes equations to analyze an axisymmetric Mach 2.0 external compression inlet from the freestream back to the flow plug. He studied primarily the inlet instability phenomena (commonly called buzz).

Presented as Paper 85-1211 at the AIAA/SAE/ASME/ASEE. 20th Joint Propulsion Conference, Monterey CA, July 8-10, 1985; received July 29, 1985; revision received Oct. 25, 1985.

*Engineering Specialist. Member AIAA.
†Engineer. Member AIAA.
‡Engineer.

The present analysis is nonzonal and extends the two-dimensional analysis to a full three-dimensional capability for inlet configurations. For two of the configurations analyzed, only three lateral planes of the code were used to simulate a two-dimensional centercut of the inlet. The third case was a three-dimensional model of an axisymmetric spike inlet.

II. Governing Equations

The governing equations are taken to be the unsteady, compressible, three-dimensional Navier-Stokes equations in mass-averaged variables which, in the absence of any external forces, may be expressed notationally in the following chain-rule conservative form[9]:

$$\frac{\partial U}{\partial t}+\left(\frac{\partial \xi}{\partial x},\frac{\partial \xi}{\partial y},\frac{\partial \xi}{\partial z}\right)\begin{vmatrix}\frac{\partial F}{\partial \xi}\\ \frac{\partial G}{\partial \xi}\\ \frac{\partial H}{\partial \xi}\end{vmatrix}+\left(\frac{\partial \eta}{\partial x},\frac{\partial \eta}{\partial y},\frac{\partial \eta}{\partial z}\right)\begin{vmatrix}\frac{\partial F}{\partial \eta}\\ \frac{\partial G}{\partial \eta}\\ \frac{\partial H}{\partial \eta}\end{vmatrix}+\left(\frac{\partial \zeta}{\partial x},\frac{\partial \zeta}{\partial y},\frac{\partial \zeta}{\partial z}\right)\begin{vmatrix}\frac{\partial F}{\partial \zeta}\\ \frac{\partial G}{\partial \zeta}\\ \frac{\partial H}{\partial \zeta}\end{vmatrix}=0 \tag{1}$$

Here, x,y,z are Cartesian coordinates in the axial, normal, and spanwise directions, respectively; ξ,η,ζ are the corresponding transformed coordinates in a body-oriented system where

$$U=\begin{vmatrix}\rho\\ \rho u\\ \rho v\\ \rho w\\ \rho E\end{vmatrix} \tag{2}$$

$$F=\begin{vmatrix}\rho u\\ \rho u^2+\sigma_x\\ \rho uv+\tau_{x,y}\\ \rho uw+\tau_{xz}\\ (\rho E+\sigma_x)u+\tau_{xy}v+\tau_{xz}w-q_x\end{vmatrix} \tag{3}$$

$$G=\begin{vmatrix}\rho v\\ \rho vu+\tau_{yx}\\ \rho v^2+\sigma_y\\ \rho vw+\tau_{yz}\\ (\rho E+\sigma_y)v+\tau_{yx}u+\tau_{yz}w-q_y\end{vmatrix} \tag{4}$$

$$H=\begin{vmatrix}\rho w\\ \rho wu+\tau_{zx}\\ \rho wv+\tau_{zy}\\ \rho w^2+\sigma_z\\ (\rho E+\sigma_z)w+\tau_{zx}u+\tau_{zy}v-q_z\end{vmatrix} \tag{5}$$

where

$$\sigma_x=P+\left[\frac{2}{3}\left(\mu+\mu_t\right)\left(\frac{\partial u}{\partial x}+\frac{\partial v}{\partial y}+\frac{\partial w}{\partial z}\right)-2\left(\mu+\mu_t\right)\frac{\partial u}{\partial x}\right] \tag{6a}$$

$$\sigma_y=P+\left[\frac{2}{3}\left(\mu+\mu_t\right)\left(\frac{\partial u}{\partial x}+\frac{\partial v}{\partial y}+\frac{\partial w}{\partial z}\right)-2\left(\mu+\mu_t\right)\frac{\partial v}{\partial y}\right] \tag{6b}$$

$$\sigma_z=P+\left[\frac{2}{3}\left(\mu+\mu_t\right)\left(\frac{\partial u}{\partial x}+\frac{\partial v}{\partial y}+\frac{\partial w}{\partial z}\right)-2\left(\mu+\mu_t\right)\frac{\partial w}{\partial z}\right] \tag{6c}$$

$$\tau_{xy}=\tau_{yx}=-\left(\mu+\mu_t\right)\left(\frac{\partial u}{\partial y}+\frac{\partial v}{\partial x}\right) \tag{7a}$$

$$\tau_{xz}=\tau_{zx}=-\left(\mu+\mu_t\right)\left(\frac{\partial u}{\partial z}+\frac{\partial w}{\partial x}\right) \tag{7b}$$

$$\tau_{yz}=\tau_{zy}=-\left(\mu+\mu_t\right)\left(\frac{\partial v}{\partial z}+\frac{\partial w}{\partial y}\right) \tag{7c}$$

$$q_x=\gamma\left(\frac{\mu}{Pr}+\frac{\mu_t}{Pr_t}\right)\frac{\partial e}{\partial x} \tag{8a}$$

$$q_y=\gamma\left(\frac{\mu}{Pr}+\frac{\mu_t}{Pr_t}\right)\frac{\partial e}{\partial y} \tag{8b}$$

$$q_z=\gamma\left(\frac{\mu}{Pr}+\frac{\mu_t}{Pr_t}\right)\frac{\partial e}{\partial z} \tag{8c}$$

$$E=e+(u^2+v^2+w^2)/2 \tag{9}$$

Effects of turbulence are incorporated by assigning $Pr_t=0.9$ and by specifying μ_t according to a simple algebraic turbulence closure model. For this purpose, the two-layer formulation developed by Baldwin-Lomax[10] was employed.

The three-dimensional, time-dependent Navier-Stokes code used in this study is a modification of the code developed by Shang.[11] The equations are solved by the well-known explicit, predictor-corrector finite difference algorithm of MacCormack.[12]

III. Boundary Conditions

The Navier-Stokes equations are elliptic in space and parabolic in time; therefore, both boundary and initial conditions must be specified.

Inflow Boundary

At the inflow boundary, all flow quantities are set equal to the freestream values. The exception to this is configuration 1, where the inflow was specified from the two-dimensional shock tables to simulate a double ramp upstream of the computational boundary. Boundary-layer effects were neglected for this case. Since all the tests were for a supersonic freestream, fixed upstream boundary conditions are physically correct.

Far-field Boundary

At the outer boundary, a freestream and zero-gradient condition were applied. This condition would allow a shock wave to pass through the outer boundary if necessary. However, for most cases tested, the outer boundary was placed sufficiently far from the inlet so that the shock wave did not intersect.

Ramp and Cowl Surfaces

The no-slip boundary condition was applied to the ramp, spike, and cowl surfaces, where $u=v=w=0$ and $\partial P/\partial n=0$. The wall temperature was specified. For cases requiring ramp bleed, mass flux and pressure were specified at the surface grid points. Two methods were used for the density boundary condition in the bleed region. The first method specified the density in the bleed region. The second method computed the density from the condition that entropy remains constant along streamlines, i.e., $Ds/Dt=0$ (see Ref. 15).

Outflow Boundary

The outflow boundary can be divided into two distinct regions separated by the grid branch cut (Fig. 1). The outer external flow region is predominantly supersonic and can be handled with the simple zero-gradient boundary condition. On the other hand, the internal duct region is primarily subsonic flow. To avoid having to specify some flow qunatity, as is typically done for subsonic outflow, a controllable exit nozzle (flow plug) is placed near the duct exit. This controllable exit nozzle chokes the subsonic duct flow to supersonic flow. The supersonic exit flow can then be handled easily with a zero-gradient condition. This technique offers many advantages over specifying outflow boundary quantities. First of all, the question of what to specify (and at what level) is eliminated. Second, the mass flow rate through the duct can be controlled by opening or closing the exit nozzle. Third, this technique more closely models the physical experiment where the duct flow rate is controlled by an exit flow plug. This exit boundary technique becomes crucial for the axisymmetric case (configuration 3) at angle of attack. The angle of attack produces circumferential variation in flow quantities that would be difficult to prescribe.

Symmetry Plane

The symmetry plane is handled by using

$$\frac{\partial \rho}{\partial \zeta}=\frac{\partial \rho u}{\partial \zeta}=\frac{\partial \rho v}{\partial \zeta}=\frac{\partial \rho E}{\partial \zeta}=w=0$$

Initial Conditions

For the initial conditions, freestream values were set at all the grid points with the exception of setting one-dimensional normal shock estimates at the inlet opening. The remainder of the inlet is initialized by utilizing one-dimensional isentropic relations.

IV. Computational Grid

The finite difference mesh for configurations 2 and 3 are shown in Figs. 1 and 2, respectively. Both internal and external flow regions are included, where the external computational region is large enough to avoid shock reflection at the far-field boundary. The grids are generated in a subroutine whose run time is negligible, so that geometric changes can easily be made during the iteration sequence. For example, the cowl setting with respect to the spike is continuously changed during a wind tunnel test. An additional benefit is that grid points need not be stored for a majority of restart cases, which saves considerable disk storage space. The cowl surface was simulated by placing a branch cut in the grid (Fig. 1). The computational flow plug uses a cubic curve fit with matching slopes at the duct interface. The throat is easily changed by specifying the minimum area.

V. Results

Configuration 1 (Two-Dimensional Generic Mach 2.2 Inlet)

Figure 3 shows the two-dimensional, Mach 2.2 generic inlet configuration. The first ramp is 6 deg, followed by a 14.4-deg second ramp. The computational domain starts just downstream of the second ramp and ends at a flow plug just beyond the entrance region. The grid size is $52\times38\times3$ and required approximately 2400 iterations to converge. Our

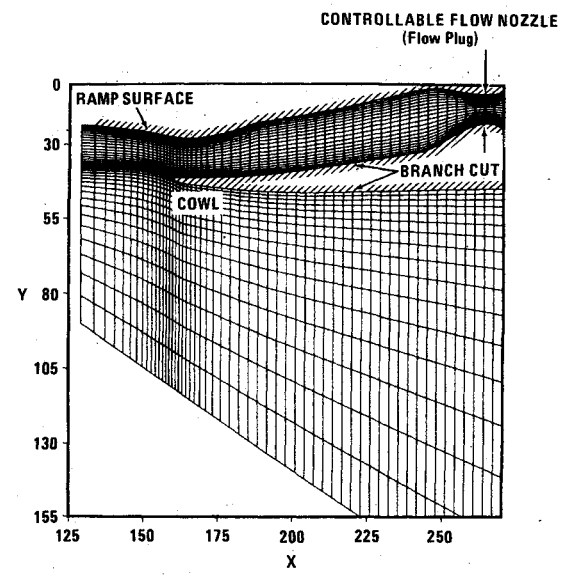

Fig. 1 F16/79 inlet grid 56×38 (configuration 2).

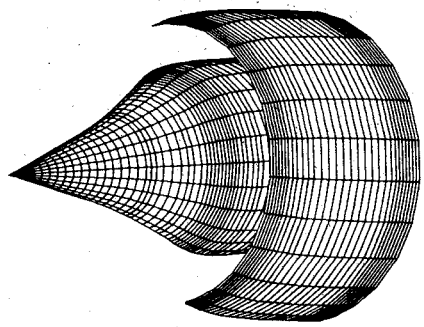

Fig. 2a Three-dimensional view of spike and cowl (configuration 3).

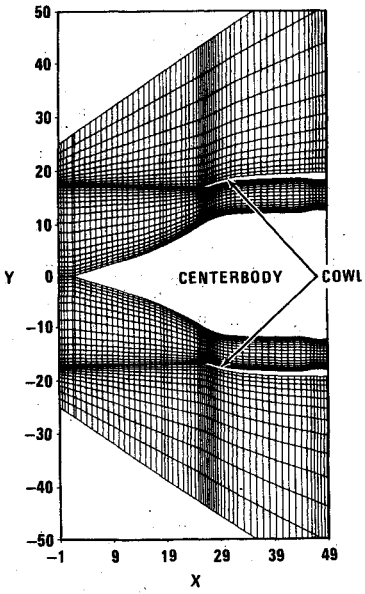

Fig. 2b Grid for spike inlet (configuration 3) planar view of grid.

criterion for convergence was that the mass flow in the inlet approach a constant value, thereby indicating a steady shock position. Experience showed this to be a reliable condition for convergence. The time per iteration was approximately 0.5 s on a CRAY computer. The surface pressure distribution on the inner cowl wall is very close to the normal-shock values, whereas the ramp pressures inside the duct vary about the normal-shock level and are affected by the ramp bleed. The Mach contours (Fig. 4) show the final shock near the ramp

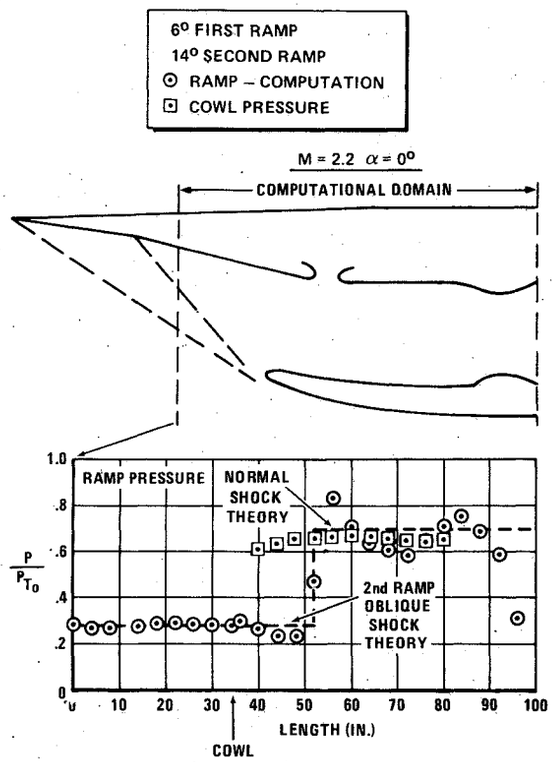

Fig. 3 Static pressure distribution on ramp and cowl for Mach 2.2 generic inlet (configuration 1) at $\alpha = 0$.

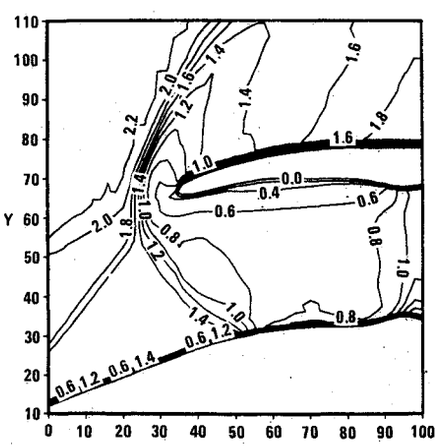

Fig. 4 Mach number contours for Mach 2.2 generic inlet (configuration 1) at $\alpha = 0$.

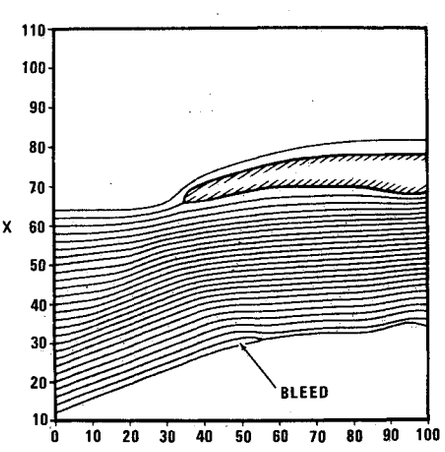

Fig. 5 Particle paths for Mach 2.2 generic inlet (configuration 1) at $\alpha = 0$.

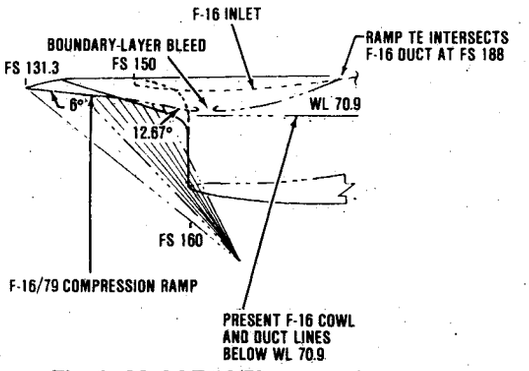

Fig. 6 Model F-16/79 compression ramps.

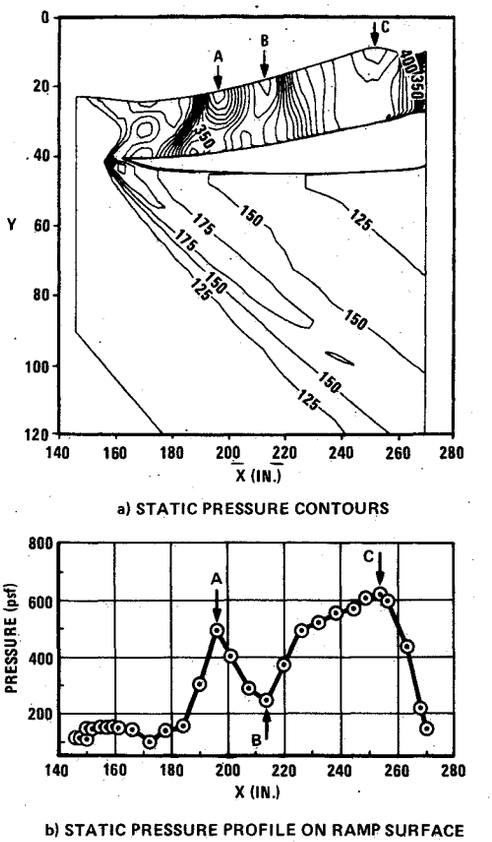

Fig. 7 Supercritical inlet flow in normal-shock inlet.

surface to be slightly oblique, which explains the decrease in pressure below the normal-shock value. Particle path traces in the inlet are shown in Fig. 5.

Configuration 2 (Two-Dimensional F-16/79 Inlet, Mach 2.0, $\alpha = 0$)

This case represents a three-plane (two-dimensional) center-cut analysis of the F-16/79 inlet at Mach 2.0. The differences between the F-16 and F-16/79 inlet are shown in Fig. 6. The F-16/79 inlet was designed for higher Mach number performance,[13] with an inlet ramp extended approximately 20 in. for more efficient compression and a bleed system to stabilize the shock.

Inlets operate in a range of airflows from supercritical to critical to subcritical. Supercritical airflows occur at high engine mass flows, where the flow chokes at the inlet throat, goes supersonic, and finally goes through the normal-shock system well inside the inlet duct. There is usually a viscous interaction associated with this phenomena,[14] which can form "viscous throats," which in turn cause a shock train of nor-

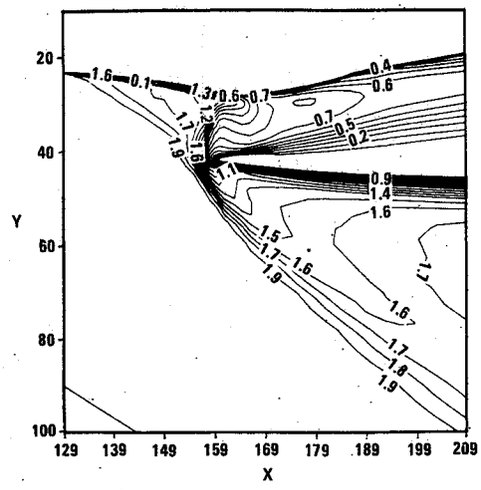

Fig. 8 Mach number contours for near-critical F-16/79.

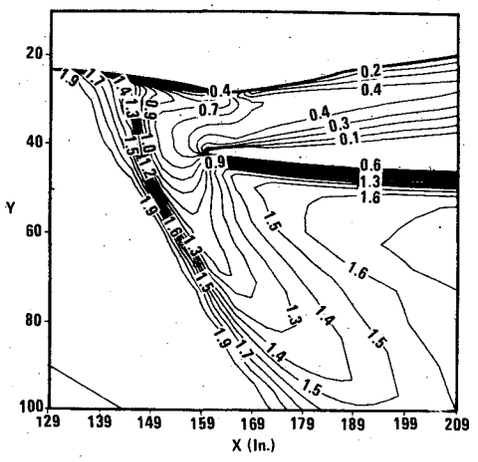

Fig. 11 Mach number contours for supercritical flow in F-16/79 inlet.

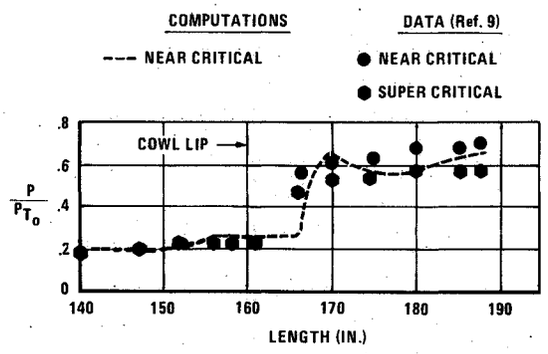

Fig. 9 Static pressure distributions on F-16/79 inlet ramp (configuration 2).

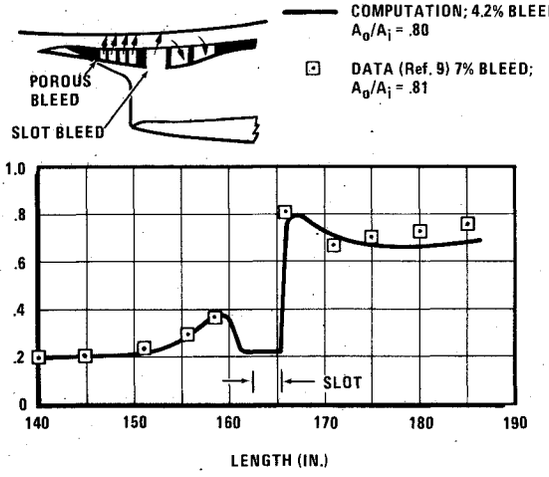

Fig. 12 Pressure distribution on F-16/79 inlet ramp surface for slot bleed case.

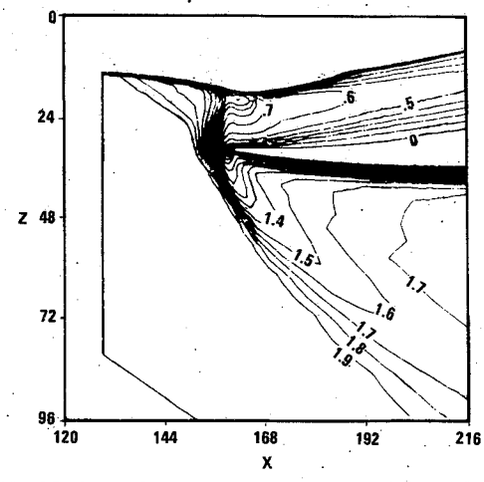

Fig. 10 Mach number contours for subcritical F-16/79 inlet.

mal shocklets (pseudoshocks). In some cases, the choked throat may not be at the geometric throat but in a location where the viscous region is separated. This case is illustrated in Fig. 7, where the supersonic flow fills a substantial portion of the entrance region of a typical normal-shock inlet. Figure 7 also shows the flow going through an expansion-compression cycle before the terminal normal shock, starting at $x = 214$ in. This type of pressure distribution is typical of those found in high-speed supercritical inlets.

The critical case is the demarcation point that divides the subcritical and supercritical inlet flows, and represents the case in which the supersonic flow is essentially all blown out of the inlet. The computational Mach contours for this case are shown in Fig. 8, and the corresponding pressure distribution labeled "near-critical" is shown in Fig. 9. Figure 10 is a subcritical case ($A_o/A_i = 0.80$), where the shock is further upstream than the near-critical shock, indicating more inlet spillage. A very subcritical flow (Fig. 11), caused by closing down the flow plug area, shows the shock being pushed further upstream to spillage levels on the verge of buzz onset.

Effects of Ramp Bleed

The mechanism of ramp bleed was modeled by two different methods. The first method specified the mass flux, pressure, and density in the bleed region. These quantities were taken to be the experimental bleed plenum values. Figure 12 shows the corresponding ramp static pressure distribution for the subcritical case ($A_o/A_i = 0.80$) shown in Fig. 10. This test case used the first method to simulate slot bleed. The predicted ramp pressures are in good agreement with the data; however, the pressures downstream of the slot were underpredicted by about 8%. A variation of the first bleed model specified the density in the bleed region by using the condition $\partial\rho/\partial n = 0$. This condition overpredicted wall pressures considerably. Evidently the bleed plenum pressure and density dominate the slot flowfield region.

The second method was similar to the first method in that the mass flux and pressure were specified. However, the density was computed from the relation $Ds/Dt = 0$. From a physical standpoint, this method seems to be more correct (Ref.

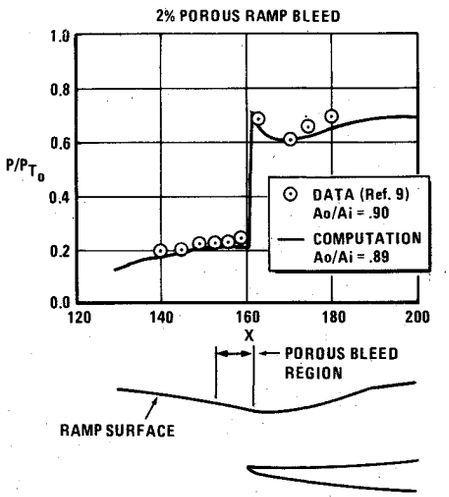

Fig. 13 Pressure distribution on ramp surface of F-16/79 inlet.

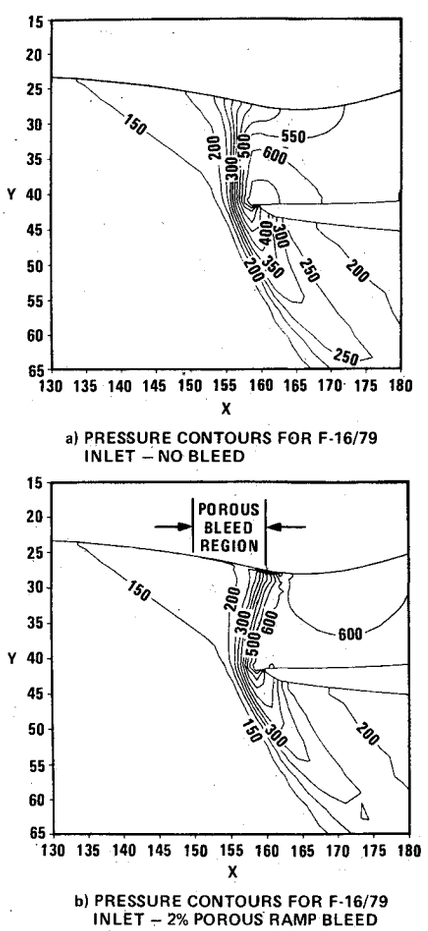

Fig. 14 Effect of ramp bleed on shock position.

15). The results of this bleed model are shown in Fig. 13 for a 2%-porous-bleed case. Predicted ramp pressures are in good agreement with test data. Figure 14 shows a comparison of this 2%-ramp-bleed case with a no-bleed case and shows the difference in the shock position as a result of the bleed.

Numerically, the porous-ramp bleed and the slot bleed are implemented in the same manner. The difference lies in where the bleed is applied. However, experimentally the two regions are different in that slot bleed is a relatively large gap in the ramp surface while porous bleed consists of small holes in the ramp surface.

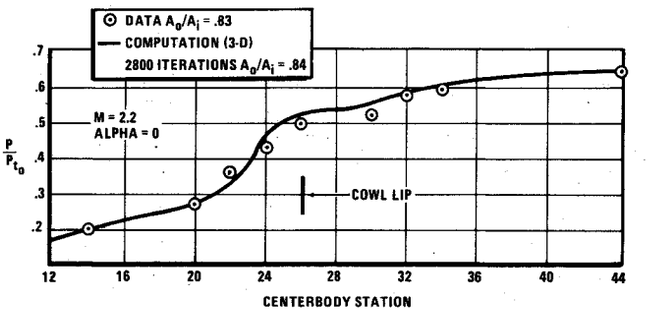

Fig. 15 Comparison of static pressures on the spike inlet centerbody at Mach 2.2, $\alpha = 0$.

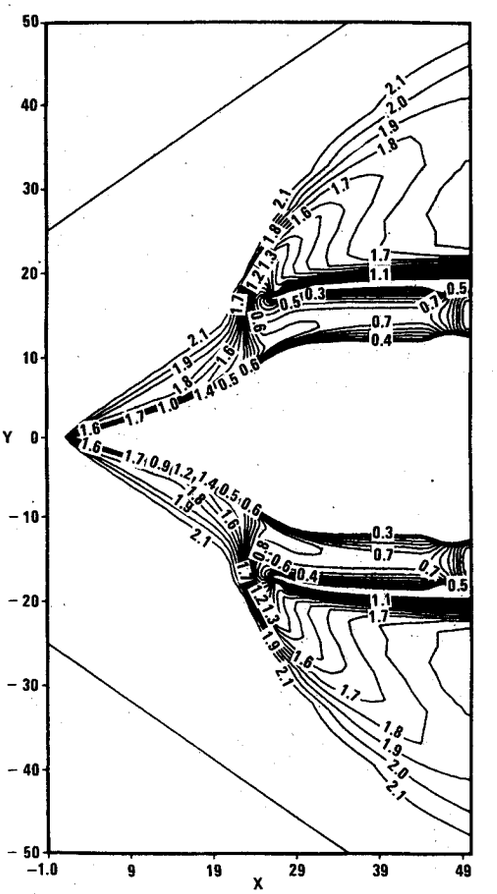

Fig. 16 Mach number contours for spike inlet at Mach 2.2, $\alpha = 0$.

Configuration 3 (Three-Dimensional Spike Inlet Mach 2.2, $\alpha = 0$)

The grid for this case is shown in Fig. 2 and was rotated 180 deg to generate the three-dimensional grid. The circumferential planes are not equally spaced and are packed closer to the $\theta = 0$ and 180 deg planes for more accurate symmetry boundary condition where $w = 0$.

At Mach 2.2 at $\alpha = 0$, a converged solution was obtained in approximately 2400 iterations. Angle-of-attack cases (not reported herein) that use the zero-angle-of-attack case as a restart converged somewhat faster. The grid size for this configuration was $64 \times 30 \times 15$ and took approximately six times longer than the two-dimensional case. Figure 15 shows the centerbody spike pressures in front of, and in the entrance region of, the inlet. The computations are in good agreement with the data. In addition, the predicted pressure recovery at the inlet throat was 0.84, while the experimental value was 0.82 at the compressor face, where additional duct loss is expected. The Mach number contour plots are shown in Fig. 16.

The angle-of-attack results are also in good agreement with the data and will be reported in a subsequent publication.

VI. Conclusions

A CFD analysis of supersonic inlets with and without bleed has been accomplished for both two- and three-dimensional configurations by using the Navier-Stokes equations. The analysis couples all elements of the shock system and subsonic diffuser into a single computational space, which is controlled by the downstream throttle setting. The computational flow plug was necessary to obtain converged solutions. The pressures in the entrance regions of the inlets are in good agreement with the data for both the two- and three-dimensional cases.

The two-dimensional solutions allowed for much computational experimentation at minimal cost before launching into the full three-dimensional computational program. The use of a three-plane, two-dimensional approximation greatly facilitated the extension to three-dimensional configurations. Configurations 1 and 2 each took approximately one man-month to complete. However, the three-dimensional solution (configuration 3) took only six man-days from the beginning of the grid generation to the converged solution reported herein.

This reduced solution time shows not only that we gained experience from the first two cases but more significantly that CFD turnaround time can have a timely impact in the design process.

The next step in the simulation process is to extend the diffuser to the compressor face and compare the total pressure distribution for both nominal attitude and angle-of-attack cases.

References

[1]"British Aerospace Seek Funds to Study HOTOL Satellite Launcher," *Aviation Week*, June 3, 1985, pp. 356-357.

[2]Knight, D., "Numerical Simulation of Realistic High-Speed Inlets Using the Navier-Stokes Equations," *AIAA Journal*, Vol. 15, Nov. 1977, pp. 1583-1589.

[3]Roberts, D. and Forester, C., "Parabolic Procedure for Flows in Ducts with Arbitrary Cross Section," *AIAA Journal*, Vol. 17, Jan. 1979, pp. 22-40.

[4]Benson, T. and Anderson B., "Validation of a Three-Dimensional Viscous Flow Analysis of Axisymmetric Supersonic Inlet Flow Fields," AIAA Paper 83-0540, 1983.

[5]Anderson, B. and Towne, C., "Numerical Simulation of Supersonic Inlets Using a Three-Dimensional Viscous Flow Analysis," AIAA Paper 80-0384, 1980.

[6]Buggeln, R., McDonald, H., Kreslovsky, J., and Levy, R., "Computation of Three-Dimensional Viscous Supersonic Flow Inlets," AIAA Paper 80-0194, Jan. 1980.

[7]Campbell, A. and Syberg, J., "Design Study of an External Compression Supersonic Inlet Using a Finite Difference Two-Dimensional Navier-Stokes Code," AIAA Paper 84-1275, 1984.

[8]Newsome, R. W., "Numerical Solutions for Steady and Unsteady Oscillatory Flow about an Axisymmetric Inlet," AFWAL-TR-83-3058, 1983.

[9]Rizzetta, D.P. and Shang, J.S., "Numerical Simulation of Leading-Edge Vortex Flows," AIAA Paper 84-1544, June 1984.

[10]Baldwin, B. and Lomax, H., "Thin Layer Approximation and Algebraic Model for Separated Turbulent Flows," AIAA Paper 78-257, 1978.

[11]Shang, J.S., "Numerical Simulation of Wing-Fuselage Interference," AIAA Paper 81-0048, Jan. 1981.

[12]MacCormack, R.W., "The Effect of Viscosity in Hypervelocity Impact Cratering," AIAA Paper 69-354, April-May 1969.

[13]Hunter, L.G. and Cawthon,, J.A., "Improved Supersonic Performance Design for the F-16 Inlet Modified for the J-79 Engine," AIAA Paper 84-1272, 1984.

[14]Hunter, L.G., "The Study of Normal Shocks (Pseudo-Shocks) with Application to Supersonic Diffusers," AFWAL-TM-82-184, Air Force Wright Aeronautical Laboratories, WPAFB, OH, 1981.

[15]Hunter, L.G., Tripp, J.M., and Howlett, D.G., "A Mach 2.0 Plus Supersonic Inlet Study Using the Navier-Stokes Equations," AIAA Paper 85-1211, 1985.